

Barycentric interpolation formulas for the sphere and the disk

Michael Chiwere^{*,†} and Grady B. Wright^{*}

Abstract

Spherical and polar geometries arise in many important areas of computational science, including weather and climate forecasting, optics, and astrophysics. In these applications, tensor-product grids are often used to represent unknowns. However, interpolation schemes that exploit the tensor-product structure can introduce artificial boundaries at the poles in spherical coordinates and at the origin in polar coordinates, leading to numerical challenges, especially for high-order methods. In this paper, we present new bivariate trigonometric barycentric interpolation formulas for spheres and bivariate trigonometric/polynomial barycentric formulas for disks, designed to overcome these issues. These formulas are also efficient, as they only rely on a set of (precomputed) weights that depend on the grid structure and not the data itself. The formulas are based on the Double Fourier Sphere (DFS) method, which transforms the sphere into a doubly periodic domain and the disk into a domain without an artificial boundary at the origin. For standard tensor-product grids, the proposed formulas exhibit exponential convergence when approximating smooth functions. We provide numerical results to demonstrate these convergence rates and showcase an application of the spherical barycentric formulas in a semi-Lagrangian advection scheme for solving the tracer transport equation on the sphere.

1 Introduction

Spherical and polar geometries are central to many important areas of computational science, including climate modeling and weather forecasting [27], geodynamics [24], cosmology [33], material science [28], optics [39], and astrophysics [25]. A key computational challenge that arises in many of these applications is interpolation, which is essential for such tasks as coupling models, filling in gaps between observations, evaluating numerical simulations at arbitrary points, and constructing surrogate models of complicated physical processes. Tensor-product spherical or polar grids are commonly employed in these applications due to their straightforward implementation, ease for visualization, alignment with geographic coordinates (in the case of the sphere), natural handling of boundary conditions and symmetries, direct mapping to computer memory layouts, and efficiency and accuracy in performing spectral transforms on the sphere [50] and disk [34].

However, these grids also present challenges for interpolation, particularly for high-order accurate methods. One major challenge is that interpolation schemes that directly exploit the tensor-product grid structure introduce artificial boundaries at the north and south poles of the spherical coordinate system and at the origin of the polar coordinate system—collectively known as the “pole problem” [12, Ch. 18]. The Double Fourier Sphere (DFS) method, first proposed by Merilees [41], addresses this issue by transforming the sphere into a doubly periodic domain (i.e., a torus) and the disk into a domain without an artificial boundary at the origin. This transformation makes it possible to apply high-order methods based on bivariate trigonometric polynomial approximations in latitude-longitude coordinates for the sphere [58] and bivariate approximations based on trigonometric and algebraic polynomials in angular-radial coordinates that are smooth over the entire disk [62].

While the DFS method forms the foundation of many high-order accurate techniques for solving a wide-range of problems (e.g., [11, 15, 21, 23, 37, 46, 53–55, 58, 62, 64, 65]), there has been surprisingly

^{*}Boise State University, Department of Mathematics, 1910 University Drive, Boise, ID 83725-1555 (michaelchiwere@u.boisestate.edu, gradywright@boisestate.edu).

[†]Corresponding author.

little focus on deriving barycentric interpolation formulas from this approach.¹ This paper aims to address this gap by developing the first bivariate barycentric interpolation formulas for the sphere and disk that work directly with the sampled data on tensor-product spherical or polar grids.

Barycentric interpolation formulas have gained significant popularity over the past 20 years, particularly following the influential review by Berrut and Trefethen [9]. While their paper focused primarily on polynomial interpolation, trigonometric analogs have existed since the earlier works of de la Vallée Poussin [16], Salzer [49], Henrici [30], and Berrut [6]. One key advantage of barycentric interpolation formulas is that they are formulated in terms of a set of weights that only depend on the locations of the sampled data, making the method straightforward to implement. These weights are also known for many common grids (e.g., equally spaced and Chebyshev) or can be precomputed and reused for any new set of data. This makes the formulas efficient to evaluate, requiring $O(kn)$ operations for n grid points and k evaluation points, compared to methods based coefficient expansions of algebraic or trigonometric polynomials which require $O(n \log n + kn)$ when the grid points are conducive to fast transforms or $O(n^2 + kn)$ when they are not. Additionally, barycentric polynomial interpolation is known to be numerically stable [32]. While stability of the barycentric trigonometric formulas can be an issue, in most cases of practical interest one does not typically encounter issues for equispaced points [3].

Our goal is to use these trigonometric and polynomial barycentric formulas with the DFS technique to derive new bivariate barycentric interpolation formulas for the sphere and disk that avoid the pole problem. The derivation leverages the symmetry properties induced by the DFS transformation, along with the barycentric formulas developed by Berrut [6] for interpolating even and odd functions. The new methods are applicable to rather general tensor-product grids, but we focus our derivation on specific grids that are commonly used in practical applications.

There are several existing techniques for approximation on the sphere and disk that also avoid the pole problem. These include splines (e.g., [2, 51]), moving least squares (e.g., [38, 60]), and radial basis functions (e.g., [22, 31]). These methods are more flexible in that they can be used for both structured and unstructured grids. However, achieving high-order accuracy with splines and moving least squares can be challenging, and there can be numerical instabilities issues with radial basis functions when taking them to higher-order (see [22, Ch. 3] more details). This can be especially problematic for tensor product grids where the points are highly anisotropic near the poles. In contrast, the interpolation formulas we derive converge faster than any polynomial order with increasing grid size for samples of smooth functions, and they avoid numerical instabilities typically associated with solving linear systems.

Finally, to highlight the advantages of the new interpolation formulas for the sphere, we apply them within a semi-Lagrangian advection (SLA) scheme to solve the tracer transport equation on the sphere. Accurate solutions of this equation are critical, as global atmospheric flows are dominated by horizontal transport. SLA techniques are widely used in atmospheric sciences to simulate not only tracer transport, but more complex non-linear shallow water flows [56]. A key step in SLA methods is interpolation, and while higher-order accurate methods have been developed for other aspects of these schemes [37, 47, 65], interpolation is done using low order methods (e.g., bivariate cubic polynomials). Our application of the new barycentric formulas demonstrates that incorporating high-order methods also for interpolation can significantly improve the solution accuracy when solving the transport equation.

The remainder of the paper is structured as follows: First, we review the DFS method and the symmetries it induces in Section 2. We then derive the bivariate trigonometric barycentric interpolation formulas for the sphere in Section 3, followed by the formulas for the disk in Section 4. Both sections contain numerical experiments demonstrating the accuracy of these formulas. We present an application of the new spherical interpolation formulas to solving the transport equation on the sphere using SLA in Section 5. Concluding remarks and a discussion of future directions are given in Section 6.

¹We note that the paper [8] does derive a barycentric formula for the disk, but it is not based on the DFS method and treats the origin of the disk as an artificial boundary.

2 The Double Fourier Sphere (DFS) method

The DFS method was first proposed by Merilees [41] for approximation on spheres and has since undergone several developments [11, 15, 21, 46, 58, 64], with more recent studies on its convergence properties [42], generalization to d -dimensional manifolds [43], and extension to solving surface PDEs [23]. The central idea of the method is to transform a function on the sphere to one on a rectangular domain, while preserving the periodicity of the function in both the azimuthal and polar directions. While this transformation results in an apparent “doubling-up” of the function, it opens up the possibility of using bivariate trigonometric (i.e., Fourier) expansions for approximating functions on the sphere. These properties are why the method is called the DFS method.

The transform introduced by the DFS method can be described as follows [58]. Let (x, y, z) be a point on the unit sphere² and parameterized in spherical coordinates as

$$x = \cos \phi \sin \theta, \quad y = \sin \phi \sin \theta, \quad z = \cos \theta, \quad (\lambda, \theta) \in [0, 2\pi] \times [0, \pi],$$

where ϕ and θ are the azimuthal and polar coordinates, respectively. A function $f(x, y, z)$ on a sphere is transformed to these coordinates as

$$f(\phi, \theta) = f(\cos \phi \sin \theta, \sin \phi \sin \theta, \cos \theta), \quad (\phi, \theta) \in [0, 2\pi] \times [0, \pi]. \quad (1)$$

However, while the transformed function is 2π periodic in ϕ , artificial boundaries have been introduced in θ at 0 and π , and the inherent periodicity in this coordinate has been destroyed. To recover periodicity in θ , the DFS method associates f with the following “doubled-up” function on $[0, 2\pi] \times [-\pi, \pi]$:

$$\tilde{f}(\phi, \theta) = \begin{cases} g(\phi, \theta), & (\phi, \theta) \in [0, \pi] \times [0, \pi], \\ h(\phi - \pi, \theta), & (\phi, \theta) \in [\pi, 2\pi] \times [0, \pi], \\ g(\phi - \pi, -\theta), & (\phi, \theta) \in [\pi, 2\pi] \times [-\pi, 0], \\ h(\phi + \pi, -\theta), & (\phi, \theta) \in [0, \pi] \times [-\pi, 0], \end{cases} \quad (2)$$

where $g(\phi, \theta) = f(\phi, \theta)$ and $h(\phi, \theta) = f(\phi + \pi, \theta)$ for $(\phi, \theta) \in [0, \pi] \times [0, \pi]$. The new function \tilde{f} has the properties that $\tilde{f}(\phi, \theta) = f(\phi, \theta)$ for $(\phi, \theta) \in [0, 2\pi] \times [0, \pi]$ and $\tilde{f}(\phi, \theta) = f(\phi - \pi, -\theta)$ for $(\phi, \theta) \in [0, 2\pi] \times [0, \pi]$. This last relationship is referred to as a *glide reflection*. The function \tilde{f} is 2π -periodic in both ϕ and θ and constant along the lines $\theta = 0$ and $\theta = \pm\pi$, which corresponds to the north and south poles. Figure 1 gives a visual summary of the DFS method.

There is a DFS analog for functions defined on a disk that have similarly gone through several developments [18, 21, 29, 53, 62]. The central idea is to transform a function on a disk to one on a rectangular domain that preserves the periodicity of the function in the polar direction and contains no artificial boundaries in the radial direction at the origin of the disk. This can be done as follows [62]. First, a function $f(x, y)$ defined in Cartesian coordinates on the unit disk³ is written in polar coordinates as

$$f(\phi, \rho) = f(\rho \cos \phi, \rho \sin \phi) \quad (\phi, \rho) \in [0, 2\pi] \times [0, 1], \quad (3)$$

where ϕ and ρ are the polar and radial coordinates, respectively. Similar to the sphere, the transformed function is 2π periodic in ϕ , but now has an artificial boundary at $\rho = 0$, which corresponds to the center of the disk. To remove this boundary, the disk counterpart to the DFS method associates f to the “doubled-up” function \tilde{f} on $[0, 2\pi] \times [-1, 1]$:

$$\tilde{f}(\phi, \rho) = \begin{cases} g(\phi, \rho), & (\phi, \rho) \in [0, \pi] \times [0, 1], \\ h(\phi - \theta, \rho), & (\phi, \rho) \in [\pi, 2\pi] \times [0, 1], \\ g(\phi - \pi, -\rho), & (\phi, \rho) \in [\pi, 2\pi] \times [-1, 0], \\ h(\phi + \pi, -\rho), & (\phi, \rho) \in [0, \pi] \times [-1, 0], \end{cases} \quad (4)$$

²Spheres of arbitrary radii can also be treated by appropriate scaling

³Disks of arbitrary radii can also be treated by appropriate scaling

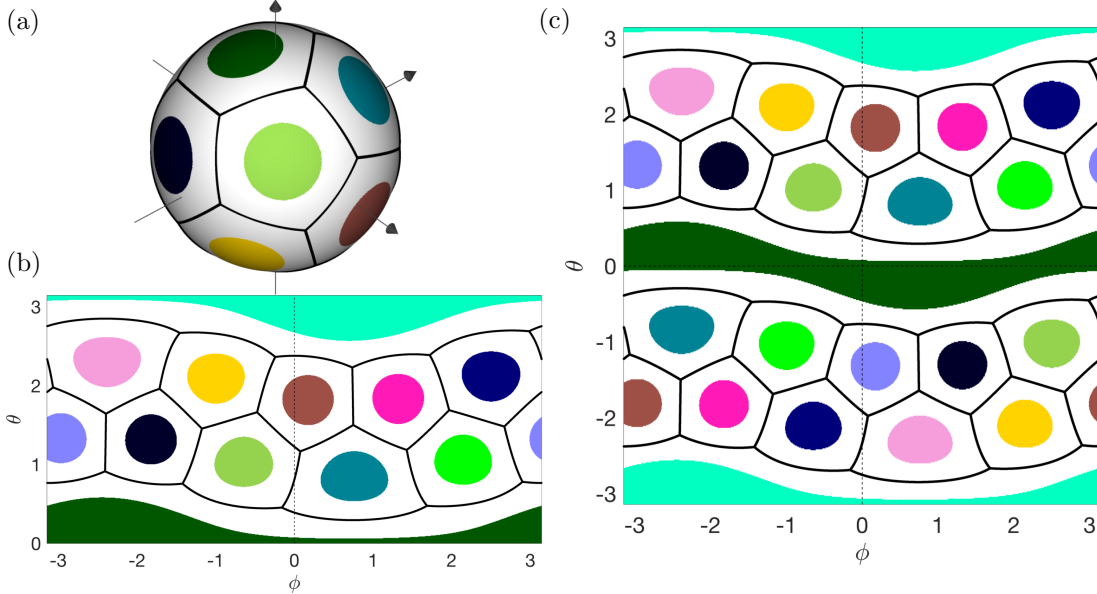


Figure 1: The DFS method applied to a football (or soccer ball) pattern on the sphere. (a) Football pattern—note the rotation to avoid symmetries with respect to the standard coordinate axes. (b) The projection of the football pattern using spherical coordinates. (c) Football pattern after applying the DFS method resulting in a doubly periodic pattern.

where $g(\phi, \rho) = f(\phi, \rho)$ and $h(\phi, \rho) = f(\phi + \pi, \rho)$ for $(\phi, \rho) \in [0, \pi] \times [0, 1]$. The new function \tilde{f} is 2π -periodic in ϕ and does not have a boundary at $\rho = 0$. Furthermore, it has a similar glide reflection property as the sphere and is constant along the line $\rho = 0$.

The disk counterpart to the DFS method also results in an apparent “doubling-up” of the function that is favorable for bivariate Fourier-polynomial approximations, such as Fourier-Chebyshev or Fourier-Legendre series. In these cases, the polynomials are defined for $\rho \in [-1, 1]$, rather than $[0, 1]$. For polynomial approximations based on interpolation at Chebyshev or Legendre points, this not only means the origin is not a boundary, but also that the interpolation points are not as clustered at the origin [21] (see also Figure 4). Note that even though the disk counterpart of the DFS method does not use bivariate Fourier series, it is still referred to as the DFS method for the disk [62].

2.1 BMC symmetry and even-periodic/odd-antiperiodic decompositions

The barycentric interpolation schemes introduced here are designed to enforce the symmetry associated with the functions \tilde{f} in both DFS methods (2) and (4) so that they can always be related back to the respective domains they are defined on. To further elucidate the symmetries associated with these functions, we use a slight abuse of notation to write them as

$$\tilde{f} = \begin{bmatrix} g & h \\ \text{flip}(h) & \text{flip}(g) \end{bmatrix}, \quad (5)$$

where `flip` refers to the MATLAB command that reverses the order of the rows of a matrix. The symmetry exhibited in (5) is referred to as *block-mirror-centrosymmetric* (BMC) symmetry [58] and can be further classified into BMC-I and BMC-II types if \tilde{f} is the extension of a function on the sphere and disk, respectively.

Definition 1. (*Block-mirror-centrosymmetric (BMC) functions* [58, 62]) A function $\tilde{f} : [0, 2a] \times [-b, b] \rightarrow \mathbb{C}$, where $a, b > 0$, is a BMC function if \tilde{f} is $2a$ periodic in its first variable and there are functions $g, h : [0, a] \times [0, b] \rightarrow \mathbb{C}$ such that \tilde{f} satisfies (5). BMC functions can further be classified as follows:

1. If \tilde{f} is $2b$ -periodic in its second argument and constant when its second argument is equal to 0 and b , then \tilde{f} is a BMC-I function.
2. If \tilde{f} is constant when the second argument is equal to 0, then \tilde{f} is a BMC-II function.

From these definitions, we see that if \tilde{f} is a BMC-I function with $a = b = \pi$, then it can be related to a function f on the sphere using the functions g and h . This function will be at least continuous on the sphere since \tilde{f} is forced to be constant at the north and south poles. A similar result holds for the disk and BMC-II functions with $a = \pi$ and $b = 1$. However, these functions are constant only at the origin, which is required for continuity. Our goal is to construct interpolation formulas that satisfy BMC symmetry and, in certain special cases, BMC-I or BMC-II symmetry so that they can be related back to the sphere or disk. Another goal of our interpolation formulas is to work only on the original functions f in (1) and (3), rather than their respective extensions (2) and (4).

Both of these goals can be realized from the following decomposition (first noted in [58]) of \tilde{f} in (5):

$$\tilde{f} = \underbrace{\frac{1}{2} \begin{bmatrix} g-h & -(g-h) \\ \text{flip}(g-h) & -\text{flip}(g-h) \end{bmatrix}}_{\tilde{f}^-} + \underbrace{\frac{1}{2} \begin{bmatrix} g+h & g+h \\ \text{flip}(g+h) & \text{flip}(g+h) \end{bmatrix}}_{\tilde{f}^+}. \quad (6)$$

For BMC-I functions $\tilde{f}(\phi, \theta)$ with $a = b = \pi$, we see from this decomposition that \tilde{f}^- is an odd 2π -periodic function in θ and π -antiperiodic⁴ in ϕ , while \tilde{f}^+ is an even 2π -periodic function in θ , π -periodic in ϕ , and constant when $\theta = 0, \pi$. The following Lemma uses this result to give conditions for the extension of a function f defined for $[0, 2\pi] \times [0, \pi]$ to have BMC-I symmetry.

Lemma 1. *Let $f : [0, 2\pi] \times [0, \pi] \rightarrow \mathbb{C}$ have the additive decomposition*

$$f(\phi, \theta) = f^-(\phi, \theta) + f^+(\phi, \theta), \quad (7)$$

where $f^-(\phi, \theta) = \frac{1}{2}(g(\phi, \theta) - h(\phi, \theta))$ and $f^+(\phi, \theta) = \frac{1}{2}(g(\phi, \theta) + h(\phi, \theta))$, with g and h taking the same definitions as in (2). If f^- is odd, 2π -periodic in θ , and π -antiperiodic in ϕ , and f^+ is even, 2π -periodic in θ , and π -periodic in ϕ , then the extension \tilde{f} of f given by (2) is a BMC function. If f^+ is furthermore constant for all ϕ when $\theta = 0, \pi$, then \tilde{f} is a BMC-I function.

Proof. The result follows directly by applying (2) to f and showing one gets (6) with the appropriate parity/periodic properties of a BMC-I function. \square

A similar result holds for the disk, but, in this case, \tilde{f}^- and \tilde{f}^+ in (6) only need to be odd and even in ρ , respectively, but not periodic. We summarize this in a similar lemma and omit the proof.

Lemma 2. *Let $f : [0, 2\pi] \times [0, 1] \rightarrow \mathbb{C}$ have the additive decomposition*

$$f(\phi, \rho) = f^-(\phi, \rho) + f^+(\phi, \rho), \quad (8)$$

where $f^-(\phi, \rho) = \frac{1}{2}(g(\phi, \rho) - h(\phi, \rho))$ and $f^+(\phi, \rho) = \frac{1}{2}(g(\phi, \rho) + h(\phi, \rho))$, with g and h taking the same definitions as in (4). If f^- is odd in ρ and π -antiperiodic in ϕ , and f^+ is even in ρ and π -periodic in ϕ , then the extension \tilde{f} of f is a BMC function. If f^+ is furthermore constant for all ϕ when $\rho = 0$, then \tilde{f} is a BMC-II function.

3 Barycentric interpolation formulas for the sphere

The plan for constructing interpolants for the sphere that preserve BMC symmetry is to construct barycentric interpolation formulas that match the parity/periodic properties of f^+ and f^- discussed in Lemma 1. These formulas can be naturally derived using a tensor product of 1D trigonometric barycentric formulas in ϕ and θ . Before deriving these formulas, we first review several commonly used tensor product grids to which these formulas are specifically tailored.

⁴ π -antiperiodic here means $\tilde{f}^-(\phi + \pi, \theta) = -\tilde{f}^-(\phi, \theta)$ for all ϕ and any θ

3.1 Common tensor product grids

We consider the following three tensor product latitude-longitude grids on the sphere: equally spaced (EQ), shifted equally spaced (SEQ), and Gauss-Legendre (GL). These are given explicitly as follows:

$$\begin{aligned} \text{EQ: } (\phi_k, \theta_j) &= \left(\frac{\pi}{m}k, \frac{\pi}{n-1}j \right), \quad k = 0, \dots, 2m-1, \quad j = 0, \dots, n-1, \\ \text{SEQ: } (\phi_k, \theta_j) &= \left(\frac{\pi}{m} \left(k + \frac{1}{2} \right), \frac{\pi}{n} \left(j + \frac{1}{2} \right) \right), \quad k = 0, \dots, 2m-1, \quad j = 0, \dots, n-1, \\ \text{GL: } (\phi_k, \theta_j) &= \left(\frac{\pi}{m}k, \arccos(z_j) \right), \quad k = 0, \dots, 2m-1, \quad j = 0, \dots, n-1. \end{aligned}$$

For the GL grid, z_j are roots of the degree n Legendre polynomial. See Figure 2 for a visual comparison of these grids.

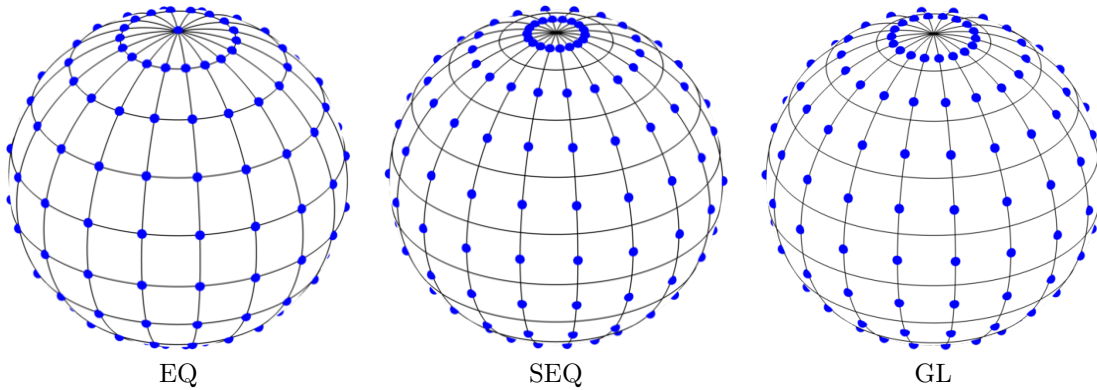


Figure 2: Illustrations of common spherical grids for which the barycentric formulas are applicable. For the EQ grid $m = n - 1 = 9$, while for the SEQ and GL grids $m = n = 9$. Grid points are marked by blue dots and the solid lines correspond to an EQ grid for reference.

The EQ and SEQ grids are used in numerical weather prediction [15, 37, 55, 64], astrophysics [5, 14, 57], and even machine learning [40]. GL grids are most commonly used for problems that employ spherical harmonics since Gaussian quadrature rules can be used to exactly integrate these basis functions [1, 26, 50].

Note that tensor product latitude-longitude grids almost always use equally spaced points in longitude, since then one can naturally use the fast Fourier transform (FFT) to speed-up certain computations in this direction (e.g., differentiation or integration). We have thus limited our focus to these cases. Our formulas also require that there are an even number of these longitude points to preserve BMC symmetry in the sampled data.

3.2 Barycentric formulas for an even or odd periodic function

Let f_j , $j = 0, \dots, n-1$ correspond to samples of an even 2π -periodic function at the set of interpolation nodes $\mathcal{S}_n = \{\theta_j\}_{j=0}^{n-1} \subseteq [0, \pi]$, where $\theta_j < \theta_{j+1}$, $j = 0, \dots, n-2$. Then there exists a unique cosine polynomial $u^c(\theta)$ of degree $n-1$ that interpolates this data and can be written in Lagrange form as [66]

$$u^c(\theta) = \sum_{j=0}^{n-1} \frac{\prod_{i=0, i \neq j}^{n-1} (\cos \theta - \cos \theta_j)}{\prod_{i=0, i \neq j}^{n-1} (\cos \theta_j - \cos \theta_i)} f_j. \quad (9)$$

With the aim of reducing the computational cost of this formula, Berrut [6] derived the equivalent barycentric formula⁵:

$$u^c(\theta) = \frac{\sum_{j=0}^{n-1} \frac{w_j}{\cos \theta - \cos \theta_j} f_j}{\sum_{j=0}^{n-1} \frac{w_j}{\cos \theta - \cos \theta_j}}, \quad \text{where } w_j = \left(\prod_{\substack{i=0 \\ i \neq j}}^{n-1} (\cos \theta_j - \cos \theta_i) \right)^{-1}. \quad (10)$$

If the interpolation nodes \mathcal{S}_n are evenly spaced, as is the case for the EQ and SEQ grids, then (10) simplifies into four possible cases that depend on whether 0 or π are in \mathcal{S}_n :

$$u^c(\theta) = \frac{\sum_{j=0}^{n-1} \frac{(-1)^j \delta_j \eta_j}{\cos \theta - \cos \theta_j} f_j}{\sum_{j=0}^{n-1} \frac{(-1)^j \delta_j \eta_j}{\cos \theta - \cos \theta_j}}, \quad \text{where } \eta_j = \begin{cases} \sin \theta_j, & 0 \notin \mathcal{S}_n, \pi \notin \mathcal{S}_n, \\ \cos \frac{\theta_j}{2}, & 0 \in \mathcal{S}_n, \pi \notin \mathcal{S}_n, \\ \sin \frac{\theta_j}{2}, & 0 \notin \mathcal{S}_n, \pi \in \mathcal{S}_n, \\ 1, & 0 \in \mathcal{S}_n, \pi \in \mathcal{S}_n, \end{cases} \quad \delta_j = \begin{cases} \frac{1}{2}, & \theta_j = 0 \text{ or } \theta_j = \pi, \\ 1, & \text{otherwise.} \end{cases} \quad (11)$$

If the samples f_0, \dots, f_{n-1} come instead from an odd 2π -periodic function sampled at \mathcal{S}_n , then there exists a unique sine polynomial $u^s(\theta)$ of degree $n-1$ that interpolates the data and can be written in Lagrange form as [66]

$$u^s(\theta) = \sum_{j=0}^{n-1} \frac{\sin \theta \prod_{i=0, i \neq j}^{n-1} (\cos \theta - \cos \theta_i)}{\sin \theta_j \prod_{i=0, i \neq j}^{n-1} (\cos \theta_j - \cos \theta_i)} f_j. \quad (12)$$

Berrut [6] also derived equivalent barycentric formulas for this case that again depend on whether 0 and π are in \mathcal{S}_n :

$$u^s(\theta) = \begin{cases} \sin \theta \frac{\sum_{j=0}^{n-1} \frac{w_j \sin \theta_j}{\cos \theta - \cos \theta_j} f_j}{\sum_{j=0}^{n-1} \frac{w_j \sin^2 \theta_j}{\cos \theta - \cos \theta_j}}, & 0 \in \mathcal{S}_n, \pi \in \mathcal{S}_n, \\ \sin \theta \frac{\sum_{j=0}^{n-1} \frac{w_j \csc \theta_j}{\cos \theta - \cos \theta_j} f_j}{\sum_{j=0}^{n-1} \frac{w_j}{\cos \theta - \cos \theta_j}}, & \text{otherwise,} \end{cases} \quad (13)$$

where w_j are given in (10). Similar to the even periodic formulas, when \mathcal{S}_n contains equally spaced nodes (13) simplifies considerably to

$$u^s(\theta) = \sin \theta \frac{\sum_{j=0}^{n-1} (-1)^j \frac{\xi_j}{\cos \theta - \cos \theta_j} f_j}{\sum_{j=0}^{n-1} (-1)^j \frac{\xi_j \sin \theta_j}{\cos \theta - \cos \theta_j}}, \quad \text{where } \xi_j = \begin{cases} 1, & 0 \notin \mathcal{S}_n, \pi \notin \mathcal{S}_n, \\ \sin \frac{\theta_j}{2}, & 0 \in \mathcal{S}_n, \pi \notin \mathcal{S}_n, \\ \cos \frac{\theta_j}{2}, & 0 \notin \mathcal{S}_n, \pi \in \mathcal{S}_n, \\ \sin \theta_j, & 0 \in \mathcal{S}_n, \pi \in \mathcal{S}_n. \end{cases} \quad (14)$$

We note that when \mathcal{S}_n contains transformed GL points, $\theta_j = \arccos(z_j)$, the barycentric weights in both (10) and (13) correspond to the standard standard polynomial barycentric weights for the GL points. These weights can be computed efficiently (and stably) from GL quadrature weights, or, for large n , using an explicit asymptotic formula [10]. In our work, we use the barycentric GL weights computed in the `legpts` function of `Chebfun` [17], which uses a variation of these formulas.

⁵In this formula the value of $u^c(\theta_k)$, for any $k = 0, \dots, n-1$, is understood from the limiting the behavior of the formula, which gives $u^c(\theta_k) = f_k$. This same interpretation applies to all remaining barycentric interpolation formulas presented.

3.3 Barycentric formulas for a π -periodic or π -antiperiodic function

We now consider the case where the grid points ϕ_k are equally spaced and the samples $\{f_j\}_{j=0}^{2m-1}$ come from a π -periodic or π -antiperiodic function $f(\phi)$. In both cases, f is also 2π -periodic so that the standard trigonometric barycentric formula derived by Henrici [30] could be used:

$$p(\phi) = \frac{\sum_{k=0}^{2m-1} (-1)^k \cot \frac{\phi - \phi_k}{2} f_k}{\sum_{k=0}^{2m-1} (-1)^k \cot \frac{\phi - \phi_k}{2}}. \quad (15)$$

However, we can exploit the periodicity to reduce the computational cost of this formula, since in the π -periodic case $f_{k+m} = f_k$ and in the antiperiodic case $f_{k+m} = -f_k$, for $k = 0, \dots, m-1$. The resulting π -periodic barycentric formula is trivially then just a rescaling and truncation of the sums in (15):

$$p^+(\phi) = \begin{cases} \frac{\sum_{k=0}^{m-1} (-1)^k \cot(\phi - \phi_k) f_k}{\sum_{k=0}^{m-1} (-1)^k \cot(\phi - \phi_k)}, & m \text{ even,} \\ \frac{\sum_{k=0}^{m-1} (-1)^k \csc(\phi - \phi_k) f_k}{\sum_{k=0}^{m-1} (-1)^k \csc(\phi - \phi_k)}, & m \text{ odd.} \end{cases} \quad (16)$$

The derivation of the barycentric formula for the π -antiperiodic interpolant requires a little more effort. Starting with (15) and exploiting the relationship $f_{k+m} = -f_k$, $k = 0, \dots, m-1$, we obtain

$$\begin{aligned} p^-(\phi) &= \frac{\sum_{k=0}^{m-1} \left[(-1)^k \cot\left(\frac{\phi - \phi_k}{2}\right) f_k + (-1)^{m+k} \cot\left(\frac{\phi - \phi_{k+m}}{2}\right) f_{k+m} \right]}{\sum_{k=0}^{m-1} \left[(-1)^k \cot\left(\frac{\phi - \phi_k}{2}\right) + (-1)^{m+k} \cot\left(\frac{\phi - \phi_{k+m}}{2}\right) \right]} \\ &= \frac{\sum_{k=0}^{m-1} (-1)^k \left[\cot\left(\frac{\phi - \phi_k}{2}\right) - (-1)^m \cot\left(\frac{\phi - \phi_k}{2} - \frac{\pi}{2}\right) \right] f_k}{\sum_{k=0}^{m-1} (-1)^k \left[\cot\left(\frac{\phi - \phi_k}{2}\right) + (-1)^m \cot\left(\frac{\phi - \phi_k}{2} - \frac{\pi}{2}\right) \right]} \\ &= \frac{\sum_{k=0}^{m-1} (-1)^k \left[\cot\left(\frac{\phi - \phi_k}{2}\right) + (-1)^m \tan\left(\frac{\phi - \phi_k}{2}\right) \right] f_k}{\sum_{k=0}^{m-1} (-1)^k \left[\cot\left(\frac{\phi - \phi_k}{2}\right) - (-1)^m \tan\left(\frac{\phi - \phi_k}{2}\right) \right]}, \end{aligned}$$

where in the last equality we have used $\cot(\alpha - \frac{\pi}{2}) = -\tan(\alpha)$. By further using the identities $\cot \alpha + \tan \alpha = 2/\sin(2\alpha)$ and $\cot \alpha - \tan \alpha = 2\cot(2\alpha)$, we obtain the simplified formula

$$p^-(\phi) = \begin{cases} \frac{\sum_{k=0}^{m-1} (-1)^k \csc(\phi - \phi_k) f_k}{\sum_{k=0}^{m-1} (-1)^k \cot(\phi - \phi_k)}, & m \text{ even,} \\ \frac{\sum_{k=0}^{m-1} (-1)^k \cot(\phi - \phi_k) f_k}{\sum_{k=0}^{m-1} (-1)^k \csc(\phi - \phi_k)}, & m \text{ odd.} \end{cases} \quad (17)$$

3.4 Barycentric formulas for the sphere

Let $f_{j,k}$ denote samples of a function $f(\phi, \theta)$ on one of the grids (ϕ_k, θ_j) , $j = 0, \dots, n-1$, $k = 0, \dots, 2m-1$, discussed in Section 3.1⁶. Then the samples of $f^-(\phi, \theta)$ and $f^+(\phi, \theta)$ from Lemma 1 are given as

$$f_{j,k}^- = \frac{1}{2}(f_{j,k} - f_{j,k+m}) \text{ and } f_{j,k}^+ = \frac{1}{2}(f_{j,k} + f_{j,k+m}), \quad j = 0, \dots, n-1, \quad k = 0, \dots, m-1. \quad (18)$$

To interpolate these sets of data we use bivariate trigonometric interpolants built from tensor products of the 1D formulas from the previous two sections. For the f_{jk}^- data, we combine the formulas for the π -anti-periodic interpolant in ϕ and odd periodic interpolant in θ , while for the f_{jk}^+ data, we combine the formulas for the π -periodic interpolant in ϕ and even periodic interpolant in θ . These formulas can be written respectively as

$$\begin{aligned} s^-(\phi, \theta) &= \frac{\sum_{k=0}^{m-1} (-1)^k \csc(\phi - \phi_k) u_k^s(\theta)}{\sum_{k=0}^{m-1} (-1)^k \cot(\phi - \phi_k)} \quad \& \quad s^+(\phi, \theta) = \frac{\sum_{k=0}^{m-1} (-1)^k \cot(\phi - \phi_k) u_k^c(\theta)}{\sum_{k=0}^{m-1} (-1)^k \cot(\phi - \phi_k)}, \quad \text{if } m \text{ is even,} \\ s^-(\phi, \theta) &= \frac{\sum_{k=0}^{m-1} (-1)^k \cot(\phi - \phi_k) u_k^s(\theta)}{\sum_{k=0}^{m-1} (-1)^k \csc(\phi - \phi_k)} \quad \& \quad s^+(\phi, \theta) = \frac{\sum_{k=0}^{m-1} (-1)^k \csc(\phi - \phi_k) u_k^c(\theta)}{\sum_{k=0}^{m-1} (-1)^k \csc(\phi - \phi_k)}, \quad \text{if } m \text{ is odd} \end{aligned} \quad (19)$$

where the choice for $u_k^s(\theta)$ and $u_k^c(\theta)$ in these formulas depends on the grid type, as summarized in Table 1.

To construct a barycentric trigonometric interpolant of the data f_{jk} , we combine the interpolants

⁶Note that we denote the samples of f as $f_{j,k}$ instead of $f_{k,j}$ to match the standard array indexing one uses for 2D grids, where the first index corresponds to the ‘‘vertical’’ coordinate θ and the second index corresponds to the ‘‘horizontal’’ coordinate ϕ

Grid	$u_k^c(\theta)$	$u_k^s(\theta)$
EQ	$\frac{\sum_{j=0}^{n-1} \frac{(-1)^j}{\cos \theta - \cos \theta_j} f_{j,k}^+}{\sum_{j=0}^{n-1} \frac{(-1)^j}{\cos \theta - \cos \theta_j}}$	$\sin \theta \frac{\sum_{j=0}^{n-1} \frac{(-1)^j \sin \theta_j}{\cos \theta - \cos \theta_j} f_{j,k}^-}{\sum_{j=0}^{n-1} \frac{(-1)^j \sin^2 \theta_j}{\cos \theta - \cos \theta_j}}$
SEQ	$\frac{\sum_{j=0}^{n-1} \frac{(-1)^j \sin \theta_j}{\cos \theta - \cos \theta_j} f_{j,k}^+}{\sum_{j=0}^{n-1} \frac{(-1)^j \sin \theta_j}{\cos \theta - \cos \theta_j}}$	$\sin \theta \frac{\sum_{j=0}^{n-1} \frac{(-1)^j}{\cos \theta - \cos \theta_j} f_{j,k}^-}{\sum_{j=0}^{n-1} \frac{(-1)^j \sin \theta_j}{\cos \theta - \cos \theta_j}}$
GL	$\frac{\sum_{j=0}^{n-1} \frac{w_j}{\cos \theta - \cos \theta_j} f_{j,k}^+}{\sum_{j=0}^{n-1} \frac{w_j}{\cos \theta - \cos \theta_j}}$	$\sin \theta \frac{\sum_{j=0}^{n-1} \frac{w_j \csc \theta_j}{\cos \theta - \cos \theta_j} f_{j,k}^-}{\sum_{j=0}^{n-1} \frac{w_j}{\cos \theta - \cos \theta_j}}$

Table 1: Barycentric trigonometric interpolants in latitude to the data $f_{j,k}^+$ and $f_{j,k}^-$ given in (18) for the various grids under consideration. The lower and upper prime on a summation sign means the first and last terms are halved, and the formulas for w_j are given in (10).

for s^- and s^+ as in (6), $s(\phi, \theta) = s^+(\phi, \theta) + s^-(\phi, \theta)$, and simplify to arrive at

$$s(\phi, \theta) = \begin{cases} \frac{\sum_{k=0}^{m-1} (-1)^k [\cot(\phi - \phi_k) u_k^c(\theta) + \csc(\phi - \phi_k) u_k^s(\theta)]}{\sum_{k=0}^{m-1} (-1)^k \cot(\phi - \phi_k)}, & m \text{ even,} \\ \frac{\sum_{k=0}^{m-1} (-1)^k [\csc(\phi - \phi_k) u_k^c(\theta) + \cot(\phi - \phi_k) u_k^s(\theta)]}{\sum_{k=0}^{m-1} (-1)^k \csc(\phi - \phi_k)}, & m \text{ odd.} \end{cases} \quad (20)$$

Theorem 1. *The interpolant $s : [0, 2\pi] \times [0, \pi] \rightarrow \mathbb{C}$ to the data $f_{j,k}$, $j = 0, \dots, n-1$, $k = 0, \dots, 2m-1$, sampled from a continuous function f on the sphere at the EQ, SEQ, or GL grids, is a BMC function. Furthermore, in the case of the EQ grid, s is a BMC-I function.*

Proof. The first result follows immediately from Lemma 1. The second result follows by noting that since f is continuous on the sphere, then on the EQ grid, $f_{0,k} = \beta$ and $f_{n-1,k} = \gamma$, $k = 0, \dots, 2m-1$, for some $\beta, \gamma \in \mathbb{C}$. So, $f_{0,k}^+ = \beta$, $f_{n-1,k}^+ = \gamma$, and $f_{0,k}^- = f_{n-1,k}^- = 0$, $k = 0, \dots, m$. Since $c_k(\theta)$ are interpolants, we necessarily have that $c_k(\theta_0) = c_k(0) = \beta$ and $c_k(\theta_{n-1}) = c_k(\pi) = \gamma$, $k = 0, \dots, m$. Now, s^+ is constructed from $p^+(\phi)$ in (16) and p^+ is exact for constants, thus $s^+(\phi, 0) = \beta$ and $s^+(\phi, \pi) = \gamma$ all ϕ . Finally, $s^-(\phi, 0) = s^-(\phi, \pi) = 0$ for all ϕ since all $s_k(\theta)$ are odd 2π -periodic functions. \square

Remark 1. *The interpolant (20) is also more generally applicable to other tensor product grids that use equally spaced points in longitude but different points in latitude than EQ, SEQ, or GL. The formulas in this more general case are based on c_k given in the third row of Table 1 and s_k given in (13), with the weights w_j computed according to the given points in latitude. If these latitude points contain 0 and π , then the interpolant will be a BMC-I function.*

For the EQ and SEQ grids, one can also obtain a bivariate trigonometric interpolant of a continuous function f on the sphere from the bivariate discrete Fourier transform (equivalently the FFT) of the samples of f 's DFS extension (and a doubling of the grids to cover $-\pi < \theta < 0$). From the uniqueness of the FFT [63] and the barycentric interpolant (20), these two must be equivalent. The approximation properties of (20) for the EQ and SEQ grids then follow directly from [42]. In particular, for interpolating Hölder continuous functions on the sphere one obtains algebraic rates of convergence as n and m increase, while for infinitely smooth functions, one obtains convergence rates faster than any algebraic rates.

Note that for the SEQ and GL grids that do not contain the poles ($\theta = 0$ and $\theta = \pi$) as interpolation points, the interpolant (20) is not guaranteed to be single-valued at the poles. While in practice this does not appear to degrade the convergence rates of these interpolants proved in [42], as illustrated in the next section, it could lead to issues when trying to differentiate the interpolated values in the vicinity of the poles.

We conclude by noting that a benefit of using the barycentric interpolant (20) over the equivalent interpolant written in terms of a bivariate Fourier series (cf. [58]) is that it does not require determining the Fourier coefficients. For the EQ and SEQ grids, this amounts to saving the computation of a bivariate FFT (and complex arithmetic, as used in most standard FFT algorithms). However, for the GL grid (or other grids that use non-equally spaced points in latitude), one would need to resort to a non-uniform FFT (NUFFT) (e.g. [48]), which may further increase the cost of the bivariate Fourier series approach.

3.5 Numerical example

To demonstrate that the barycentric interpolation formulas (20) work on the sphere, we consider using them to interpolate the function

$$f(\phi, \theta) = \cos(1 + 8\pi(\cos \phi + \sin \phi) \sin \theta + 5 \sin(3\pi \cos \theta)); \quad (21)$$

see Figure 3 (a) for a visualization of this function. For the numerical experiment, we select $n = m$,

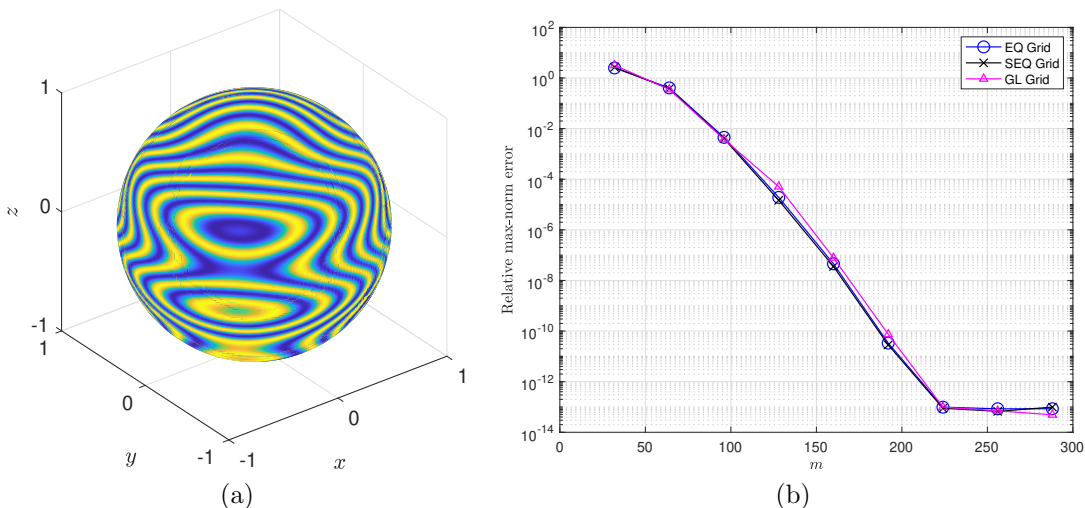


Figure 3: (a) Test function (21) on the sphere, where dark blue corresponds to -1 and bright yellow to 1. (b) Relative max-norm error in the barycentric interpolants (20) of the function in (a) for the different grids using $n = m$.

which gives $N = 2n^2$ total grid points and samples of f , and evaluate the barycentric formulas (20) at a dense set of scattered points on the sphere where we compute the relative max-norm error between s and f . Figure 3 (b) displays these errors as a function of m for each of the three grids under consideration. We see the max-norm errors are similar for each of the three different grid

types and that the errors decrease exponentially fast with m , which is expected from [42], since f is infinitely smooth.

4 Barycentric interpolation formulas for the disk

Similar to the sphere, the plan is to construct barycentric interpolation formulas for the disk that match the parity/periodic properties of f^+ and f^- discussed in Lemma 2. These will again be constructed from tensor product formulas, but now consisting of 1D trigonometric barycentric formulas in ϕ and 1D polynomial barycentric formulas in ρ . The formulas for ϕ are identical to those derived in Section 3.3, so only the 1D polynomial formulas need to be derived here. Prior to this, we first review some commonly used tensor product grids that the barycentric formulas for the disk are specifically tailored.

4.1 Common tensor product grids

We will again consider three commonly used grid types on the disk. In all the grids, the points are equally distributed in the angular direction, and we will name them depending on the nature of points in the radial direction. These are Chebyshev points of the first (CH1) and second (CH2) kinds, and Gauss-Legendre (GL) points [59]. For given positive integers m and n , we define these grids as

$$\text{CH1: } (\phi_k, \rho_j) = \left(\frac{\pi}{m}k, \cos\left(\frac{j + \frac{1}{2}}{\ell + 1}\pi\right) \right), \quad k = 0, \dots, 2m - 1, \quad j = 0, \dots, n,$$

$$\text{CH2: } (\phi_k, \rho_j) = \left(\frac{\pi}{m}k, \cos\left(\frac{j}{\ell}\pi\right) \right), \quad k = 0, \dots, 2m - 1, \quad j = 0, \dots, n,$$

$$\text{GL: } (\phi_k, \rho_j) = \left(\frac{\pi}{m}k, z_j \right), \quad k = 0, \dots, 2m - 1, \quad j = 0, \dots, n,$$

where $\ell = 2n$ if the origin is to be included ($\rho_n = 0$) in the grid or $\ell = 2n + 1$ if it is to be omitted. Also, z_j are the $n + 1$ roots in $[0, 1]$ of the degree $\ell + 1$ Legendre polynomial $P_{\ell+1}$ defined over $[-1, 1]$, and ordered so that $z_j > z_{j+1}$, $j = 0, \dots, n$. See [13] for a thorough review of applications that use these types of grids.

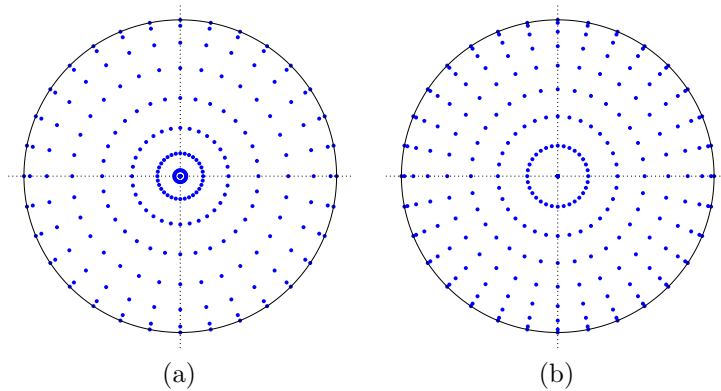


Figure 4: Comparison of Fourier-Chebyshev grids, where the points in the radial direction are (a) the Chebyshev points (of the second kind) defined over $[0, 1]$ and (b) the Chebyshev points (of the second kind) defined over $[-1, 1]$ and restricted to $[0, 1]$ as in the CH2 definition. Both grids have the same number of points in the polar and radial directions.

In all cases, the points in the radial direction ρ are the $\ell + 1$ roots or extrema in $[0, 1]$ of orthogonal polynomials defined over $[-1, 1]$. As discussed in Section 2, when the DFS method is applied to

functions sampled at these points, the full set of points over $[-1, 1]$ is recovered, allowing polynomials in ρ defined over these points to be used. As shown in Figure 4, this approach results in less clustering around the origin compared to using radial points based on roots/extrema of orthogonal polynomials defined on $[0, 1]$, as done in [8]. Furthermore, as we demonstrate in Section 4.3, this approach allows for the construction of barycentric interpolants on the disk that naturally preserve BMC symmetry.

4.2 Barycentric formulas for an even or odd function

Given samples f_j , $j = 0, \dots, \ell$, of a function f at the the interpolation points ρ_j , $j = 0, \dots, n$, the unique polynomial of degree ℓ that interpolates the data can be written in barycentric form as [9]

$$v(\rho) = \frac{\sum_{j=0}^{\ell} \frac{w_j}{\rho - \rho_j} f_j}{\sum_{j=0}^{\ell} \frac{w_j}{\rho - \rho_j}}, \quad w_j = \left(\prod_{\substack{i=0 \\ i \neq j}}^{\ell} (\rho_j - \rho_i) \right)^{-1}, \quad (22)$$

If f is even or odd and the interpolation points are symmetric about the origin, then we can exploit these symmetries to reduce the sums in determining v and the products in computing the weights to be over roughly half the terms. In deriving these formulas, we assume, without loss of generality, that $1 \geq \rho_0 > \rho_1 \cdots > \rho_\ell \geq -1$, and that $\ell = 2n$ or $\ell = 2n + 1$. In the former case, the number of interpolation points is odd, and the assumed symmetry about the origin implies that the origin is included in the point set and $\rho_n = 0$. In the latter case, the origin is not included. In either case, symmetry about the origin implies $\rho_j = -\rho_{\ell-j}$, $j = 0, \dots, n$. Similar to Section 3.2, we let $\mathcal{S}_n = \{\rho_j\}_{j=0}^n$ be the set of interpolation points that are actually used in the formulas.

We first consider the case that f is even. To derive the barycentric formula for this case, it is important to distinguish whether ℓ is even or odd. Assuming first that $\ell = 2n$, so that the origin is included, it is straightforward to show that for $j = 0, \dots, n-1$ the barycentric weights satisfy $w_j = w_{\ell-j}$, and the function samples satisfy $f_j = f_{\ell-j}$. Applying these results to (22) and denoting the interpolant as v^e gives:

$$\begin{aligned} v^e(\rho) &= \frac{\frac{w_n}{\rho - \rho_n} f_n + \sum_{j=0}^{n-1} \left[\frac{w_j}{\rho - \rho_j} f_j + \frac{w_{\ell-j}}{\rho - \rho_{\ell-j}} f_{\ell-j} \right]}{\frac{w_n}{\rho - \rho_n} + \sum_{j=0}^{n-1} \left[\frac{w_j}{\rho - \rho_j} + \frac{w_{\ell-j}}{\rho - \rho_{\ell-j}} \right]} = \frac{\frac{w_n}{\rho} f_n + \sum_{j=0}^{n-1} w_j \left[\frac{1}{\rho - \rho_j} + \frac{1}{\rho + \rho_j} \right] f_j}{\frac{w_n}{\rho} + \sum_{j=0}^{n-1} w_j \left[\frac{1}{\rho - \rho_j} + \frac{1}{\rho + \rho_j} \right]} \\ &= \frac{\frac{\rho w_n}{\rho^2} f_n + \sum_{j=0}^{n-1} \frac{2\rho w_j}{\rho^2 - \rho_j^2} f_j}{\frac{w_n \rho}{\rho^2} + \sum_{j=0}^{n-1} \frac{2\rho w_j}{\rho^2 - \rho_j^2}} = \frac{2\rho \left(\frac{w_n}{2\rho^2} f_n + \sum_{j=0}^{n-1} \frac{w_j}{\rho^2 - \rho_j^2} f_j \right)}{2\rho \left(\frac{w_n}{2\rho^2} + \sum_{j=0}^{n-1} \frac{w_j}{\rho^2 - \rho_j^2} \right)} = \frac{\sum_{j=0}^{n'} \frac{w_j}{\rho^2 - \rho_j^2} f_j}{\sum_{j=0}^{n'} \frac{w_j}{\rho^2 - \rho_j^2}}, \end{aligned} \quad (23)$$

where the prime on the summations means that the last term is halved. One can also simplify the barycentric weights in (22) to products involving only ρ_0, \dots, ρ_n :

$$w_j = \begin{cases} \left(2 \prod_{\substack{i=0 \\ i \neq j}}^n (\rho_j^2 - \rho_i^2) \right)^{-1}, & j \neq n, \\ (-1)^{n-1} \left(\prod_{i=0}^{n-1} \rho_i^2 \right)^{-1}, & j = n. \end{cases} \quad (24)$$

These formulas can be further simplified by eliminating the common 2 in all the weights, using $\rho_n = 0$, and incorporating the division by 2 into the weights when $j = n$ in the summations to obtain:

$$v^e(\rho) = \frac{\sum_{j=0}^n \frac{w_j}{\rho^2 - \rho_j^2} f_j}{\sum_{j=0}^n \frac{w_j}{\rho^2 - \rho_j^2}}, \quad w_j = \left(\prod_{\substack{i=0 \\ i \neq j}}^n (\rho_j^2 - \rho_i^2) \right)^{-1}, \quad (25)$$

Note that while we used the ordering $\rho_j > \rho_{j+1}$, $j = 0, \dots, n-1$ to derive (25), this ordering is not necessary to use the formula.

If $\ell = 2n + 1$, then the origin is not included in the point set and it is straightforward to show that the barycentric weights in (22) satisfy $w_j = -w_{\ell-j}$, $j = 0, \dots, n$. Using this symmetry, and following a similar approach to the derivations of (23) and (24) produces the following formulas for the interpolant and weights:

$$v^e(\rho) = \frac{\sum_{j=0}^n \frac{w_j \rho_j}{\rho^2 - \rho_j^2} f_j}{\sum_{j=0}^n \frac{w_j \rho_j}{\rho^2 - \rho_j^2}}, \quad w_j = \left(\rho_j \prod_{\substack{i=0 \\ i \neq j}}^n (\rho_j^2 - \rho_i^2) \right)^{-1}.$$

By dividing out the common ρ_j factor in the denominator of the formula for the weights with the same factor in the numerator of the summations defining v^e , we obtain the same barycentric formula (25) for the interpolant and weights. Thus, (25) can be used in both cases of $\ell = 2n$ or $\ell = 2n + 1$, which correspond to $0 \in \mathcal{S}_n$ and $0 \notin \mathcal{S}_n$, respectively.

The barycentric formula for the case where f is an odd function, denoted by $v^o(\rho)$, can be derived using the same procedure as the even case, but exploiting the odd symmetry in the function samples: $f_j = -f_{\ell-j}$, $j = 0, \dots, n$. However, we derive it using a simpler approach that relies on the even formula (25); this is the analogous the approach used by Berrut [6] to derive the sine interpolation formula (13) from the cosine formula (10). If $\ell = 2n$, so that $0 \in \mathcal{S}_n$, then the unique odd degree polynomial that interpolates the data must be of degree $2n - 1$. This interpolant can be constructed by first forming the degree $2n$ even polynomial interpolant (25) to the even data $f_j \rho_j$, $j = 0, \dots, n$, and then dividing it by ρ , which gives

$$v^o(\rho) = \frac{1}{\rho} \frac{\sum_{j=0}^n \frac{w_j \rho_j}{\rho^2 - \rho_j^2} f_j}{\sum_{j=0}^n \frac{w_j}{\rho^2 - \rho_j^2}}, \quad \text{if } 0 \in \mathcal{S}_n. \quad (26)$$

If instead $\ell = 2n + 1$, so that $0 \notin \mathcal{S}_n$, then the unique odd interpolant to f_j will be of degree $2n + 1$. So, we again use the unique degree $2n$ even polynomial interpolant (25), but now for the data f_j/ρ_j , $j = 0, \dots, n$, and then multiply it by ρ :

$$v^o(\rho) = \rho \frac{\sum_{j=0}^n \frac{w_j}{\rho_j(\rho^2 - \rho_j^2)} f_j}{\sum_{j=0}^n \frac{w_j}{\rho^2 - \rho_j^2}}, \quad \text{if } 0 \notin \mathcal{S}_n, \quad (27)$$

An equivalent interpolation formula to (26) can be obtained without a division by ρ by using the result that (26) is exact for the function $f(\rho) = \rho$. Combining this formula with (27), we obtain the

following barycentric formula for samples with odd symmetry:

$$v^o(\rho) = \begin{cases} \rho \frac{\sum_{j=0}^n \frac{w_j \rho_j}{\rho^2 - \rho_j^2} f_j}{\sum_{j=0}^n \frac{w_j \rho_j^2}{\rho^2 - \rho_j^2}}, & 0 \in \mathcal{S}_n, \\ \rho \frac{\sum_{j=0}^n \frac{w_j}{\rho_j(\rho^2 - \rho_j^2)} f_j}{\sum_{j=0}^n \frac{w_j}{\rho^2 - \rho_j^2}}, & 0 \notin \mathcal{S}_n, \end{cases} \quad (28)$$

where the barycentric weights are given in (25).

When the points \mathcal{S}_n correspond to Chebyshev points of the first or second kind, the barycentric weights w_j given over $[-1, 1]$ in (22) can be computed explicitly [9] and the interpolation formulas (25) and (28) can then be simplified. We have summarized these formulas in the first two rows of Table 2 for the specific case of interpolating in the radial direction on the disk.

As noted at the end of Section 3.2, the barycentric weights in (22) for the GL points can be computed efficiently (and stably) using the `legpts` function of Chebfun [17]. These weights can then be appropriately modified for incorporation into (25) and (28).

4.3 Barycentric formulas for the disk

Let $f_{j,k}$ denote samples of a function $f(\phi, \rho)$ on the tensor product grid (ϕ_k, ρ_j) , $j = 0, \dots, n$, $k = 0, \dots, 2m - 1$. Then the samples of $f^-(\phi, \rho)$ and $f^+(\phi, \rho)$ from Lemma 2 are given as

$$f_{j,k}^- = \frac{1}{2}(f_{j,k} - f_{j,k+m}) \text{ and } f_{j,k}^+ = \frac{1}{2}(f_{j,k} + f_{j,k+m}), \quad j = 0, \dots, n, \quad k = 0, \dots, m - 1. \quad (29)$$

We use the same approach as the sphere to interpolate these sets of data and construct bivariate interpolants from tensor products of the 1D anti-periodic/periodic trigonometric formulas from Section 3.3 with the 1D odd/even polynomial formulas from the previous section. The details in the derivations of the disk formulas are similar to the sphere formulas, so we omit them and just state the result:

$$s(\phi, \rho) = \begin{cases} \frac{\sum_{k=0}^{m-1} (-1)^k [\cot(\phi - \phi_k) v_k^e(\rho) + \csc(\phi - \phi_k) v_k^o(\rho)]}{\sum_{k=0}^{m-1} (-1)^k \cot(\phi - \phi_k)}, & m \text{ even} \\ \frac{\sum_{k=0}^{m-1} (-1)^k [\csc(\phi - \phi_k) v_k^e(\rho) + \cot(\phi - \phi_k) v_k^o(\rho)]}{\sum_{k=0}^{m-1} (-1)^k \csc(\phi - \phi_k)}, & m \text{ odd}, \end{cases} \quad (30)$$

where the radial interpolants $v_k^e(\rho)$ and $v_k^o(\rho)$ are given in the Table 2.

Theorem 2. *The interpolant $s : [0, 2\pi] \times [0, 1] \rightarrow \mathbb{C}$ to the data f_{jk} , $j = 0, \dots, n$, $k = 0, \dots, 2m - 1$, sampled from a continuous function f on the disk at the CH1, CH2, or GL grids, is a BMC function. Furthermore, in the case where the grid contains $\rho = 0$, s is a BMC-II function.*

Proof. The first result follows naturally from Lemma 2 and the second follows using the same arguments as the second part of the proof of Theorem 1. \square

Grid	Origin included		Origin not included	
	$v_k^e(\rho)$	$v_k^o(\rho)$	$v_k^e(\rho)$	$v_k^o(\rho)$
CH1	$\frac{\sum_{j=0}^{n'} \frac{(-1)^j \xi_j}{\rho^2 - \rho_j^2} f_{j,k}^+}{\sum_{j=0}^{n'} \frac{(-1)^j \xi_j}{\rho^2 - \rho_j^2}}$	$\rho \frac{\sum_{j=0}^n \frac{(-1)^j \xi_j \rho_j}{\rho^2 - \rho_j^2} f_{j,k}^-}{\sum_{j=0}^{n'} \frac{(-1)^j \xi_j \rho_j^2}{\rho^2 - \rho_j^2}}$	$\frac{\sum_{j=0}^n \frac{(-1)^j \rho_j \gamma_j}{\rho^2 - \rho_j^2} f_{j,k}^+}{\sum_{j=0}^n \frac{(-1)^j \rho_j \gamma_j}{\rho^2 - \rho_j^2}}$	$\frac{\sum_{j=0}^n \frac{(-1)^j \gamma_j}{\rho^2 - \rho_j^2} f_{j,k}^-}{\rho \sum_{j=0}^n \frac{(-1)^j \rho_j}{\rho^2 - \rho_j^2}}$
	where $\xi_j = \sin\left(\frac{2j+1}{4n+2}\pi\right)$		where $\gamma_j = \sin\left(\frac{2j+1}{4n+4}\pi\right)$	
CH2	$\frac{\sum_{j=0}^{n'} \frac{(-1)^j}{\rho^2 - \rho_j^2} f_{j,k}^+}{\sum_{j=0}^{n'} \frac{(-1)^j}{\rho^2 - \rho_j^2}}$	$\rho \frac{\sum_{j=0}^{n'} \frac{(-1)^j \rho_j}{\rho^2 - \rho_j^2} f_{j,k}^-}{\sum_{j=0}^{n'} \frac{(-1)^j \rho_j^2}{\rho^2 - \rho_j^2}}$	$\frac{\sum_{j=0}^n \frac{(-1)^j \rho_j}{\rho^2 - \rho_j^2} f_{j,k}^+}{\sum_{j=0}^n \frac{(-1)^j \rho_j}{\rho^2 - \rho_j^2}}$	$\frac{\sum_{j=0}^n \frac{(-1)^j}{\rho^2 - \rho_j^2} f_{j,k}^-}{\rho \sum_{j=0}^n \frac{(-1)^j \rho_j}{\rho^2 - \rho_j^2}}$
GL	$\frac{\sum_{j=0}^n \frac{w_j}{\rho^2 - \rho_j^2} f_j}{\sum_{j=0}^n \frac{w_j}{\rho^2 - \rho_j^2}}$	$\rho \frac{\sum_{j=0}^n \frac{w_j \rho_j}{\rho^2 - \rho_j^2} f_j}{\sum_{j=0}^n \frac{w_j \rho_j^2}{\rho^2 - \rho_j^2}}$	$\frac{\sum_{j=0}^n \frac{w_j}{\rho^2 - \rho_j^2} f_j}{\sum_{j=0}^n \frac{w_j}{\rho^2 - \rho_j^2}}$	$\frac{\sum_{j=0}^n \frac{w_j}{\rho_j(\rho^2 - \rho_j^2)} f_j}{\sum_{j=0}^n \frac{w_j}{\rho^2 - \rho_j^2}}$

Table 2: Barycentric polynomial interpolants in the radial direction of the disk to the data $f_{j,k}^+$ and $f_{j,k}^-$ given in (29) for the various grids under consideration. The lower prime on a summation sign means the first term is halved, while an upper prime means the last term is halved. The formulas for w_j are given in (25). In the CH1 and CH2 cases, the points are assumed to be arranged so that $\rho_j > \rho_{j+1}$, $j = 0, \dots, n-1$.

Remark 2. *Similar to the sphere, the interpolant (30) is also more generally applicable to other tensor product grids that use equally spaced polar points, but different radial points than CH1, CH2, and GL. The formulas in this more general case are based on v_k^e and v_k^o given in the third row of Table 2. If these radial points contain 0, then the interpolant will be a BMC-II function.*

Note that if the grids do not contain the origin as interpolation points, then the interpolant (30) is not guaranteed to be single-valued there. As with the sphere grids not containing the poles, this could lead to issues when trying to differentiate the interpolated values near $\rho = 0$. However, we have not observed that the convergence rates of the interpolants are degraded in this case.

4.4 Numerical example

We use a similar numerical experiment as the sphere to demonstrate the barycentric interpolation formulas (30) work for the disk. For this case, we interpolate the target function

$$f(\phi, \rho) = \sin(21\pi(1 + \cos(\pi\rho))(\rho^2 - 2\rho^5 \cos(5(\phi - 0.11)))), \quad (31)$$

which is displayed in Figure 5. We again select $n = m$, giving $N = 2n(n+1)$ total grid points and samples of f . We compute the relative max-norm error between s and f from a dense set of scattered evaluation points over the disk. These errors are displayed as a function of m for each of the three grids under consideration in Figure 5 (b). We see the max-norm errors are nearly the same for each of the three different grid types and that the errors decrease exponentially fast with m , which is expected since f is infinitely smooth.

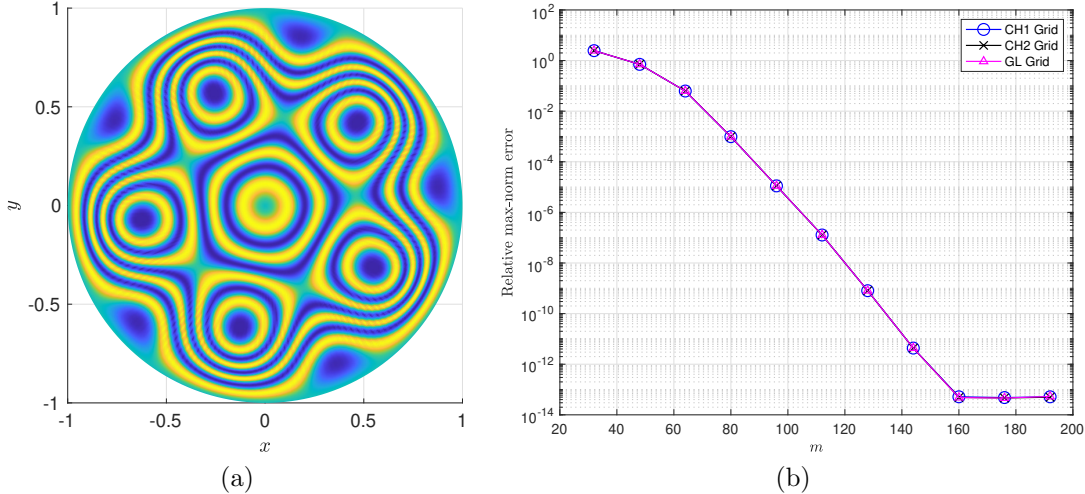


Figure 5: (a) Test function (31) on the disk, where dark blue is corresponds to -1 and bright yellow to 1. (b) Relative max-norm error in the barycentric interpolants (30) of the function in (a) for the CH1, CH2, and GL grids using $n = m$.

5 Semi-Lagrangian advection (SLA) on the sphere

In this section we combine the new spherical barycentric interpolation formulas with a SLA method to solve the tracer transport equation on the sphere. For the unit sphere \mathbb{S}^2 , this equation is given

$$\frac{\partial q}{\partial t} + \mathbf{u} \cdot \nabla_{\mathbb{S}^2} q = 0, \quad \text{or} \quad \frac{Dq}{Dt} = 0, \quad (32)$$

where q is the scalar quantity being transported, \mathbf{u} is an incompressible velocity field that is tangent to \mathbb{S}^2 , and $\nabla_{\mathbb{S}^2}$ denotes the surface gradient operator on \mathbb{S}^2 . SLA techniques have been widely used in atmospheric sciences for simulating tracer transport and more complex non-linear shallow water flows [56]. The appeal of SLA lies in its ability to avoid the strict time-step limitations of Eulerian methods, allowing for significantly larger time-steps than those dictated by the CFL condition, all while maintaining stability [19]. We follow a similar approach to [52] for testing new interpolation methods with SLA for solving (32).

The SLA scheme we consider operates as follows: we assume that a Lagrangian particle reaches each point on a fixed Eulerian grid $X = \{(\phi_j, \theta_j)\}_{j=1}^N$ at some time $t + \Delta t$, carrying a certain amount of the scalar q . The amount of q at (ϕ_j, θ_j) must have been transported in the flow field \mathbf{u} from the particle's *departure point* (ϕ_j^d, θ_j^d) at time t . To find the departure point, we trace the particle backward in time from $t + \Delta t$ to t along the flow field \mathbf{u} , then determine q by interpolating the scalar field to that departure point. Please see Algorithm 1 for an outline of this scheme. Our primary focus is on the interpolation step, while the particle trajectory will be computed using a fifth-order Runge-Kutta method (see [52] for details on this step). We use this SLA scheme with each of the three grids from Section 3.1 and use the corresponding barycentric formula (20) for the interpolation step.

5.1 Results

We consider the popular deformational flow test case from [44] to test the barycentric SLA scheme. The velocity field for this test is given as

$$u(\lambda, \theta, t) = \frac{10}{T} \cos\left(\frac{\pi t}{T}\right) \sin^2\left(\lambda - \frac{2\pi t}{T}\right) \sin(2\theta) + \frac{2\pi}{T} \cos(\theta), \quad (33)$$

$$v(\lambda, \theta, t) = \frac{10}{T} \cos\left(\frac{\pi t}{T}\right) \sin\left(2\lambda - \frac{2\pi t}{T}\right) \cos(\theta), \quad (34)$$

Algorithm 1 SLA for tracer transport on \mathbb{S}^2 using barycentric interpolation

Input: 1) $\mathbf{u}(\phi, \theta, t)$, incompressible velocity field tangent to \mathbb{S}^2 ; 2) $q(\phi, \theta, 0)$, initial tracer field; 3) $X = \{(\phi_j, \theta_j)\}_{j=1}^N$, Eulerian tensor product grid; 4) t_f , final time; 5) Δt , time-step.

Initialize $\mathbf{q}_X^0 = \{q(\phi_j, \theta_j, 0)\}_{j=1}^N$, $t = 0$, and $k = 0$.

while $t \leq t_f$ **do**

Particle-trajectory: Trace back Lagrangian particle at grid point $\mathbf{x}_j = (\phi_j, \theta_j)$ in the velocity field from $t + \Delta t$ to t to find its departure point $\mathbf{x}_j^d = (\phi_j^d, \theta_j^d)$, for $j = 1, \dots, N$.

Interpolation: Interpolate \mathbf{q}_X^k to $X^d = \{(\phi_j^d, \theta_j^d)\}_{j=1}^N$ using barycentric interpolation formula (20) to obtain $\mathbf{q}_{X^d}^k$.

Update $\mathbf{q}_X^{k+1} = \mathbf{q}_{X^d}^k$, $k = k + 1$, and $t = k\Delta t$.

end while

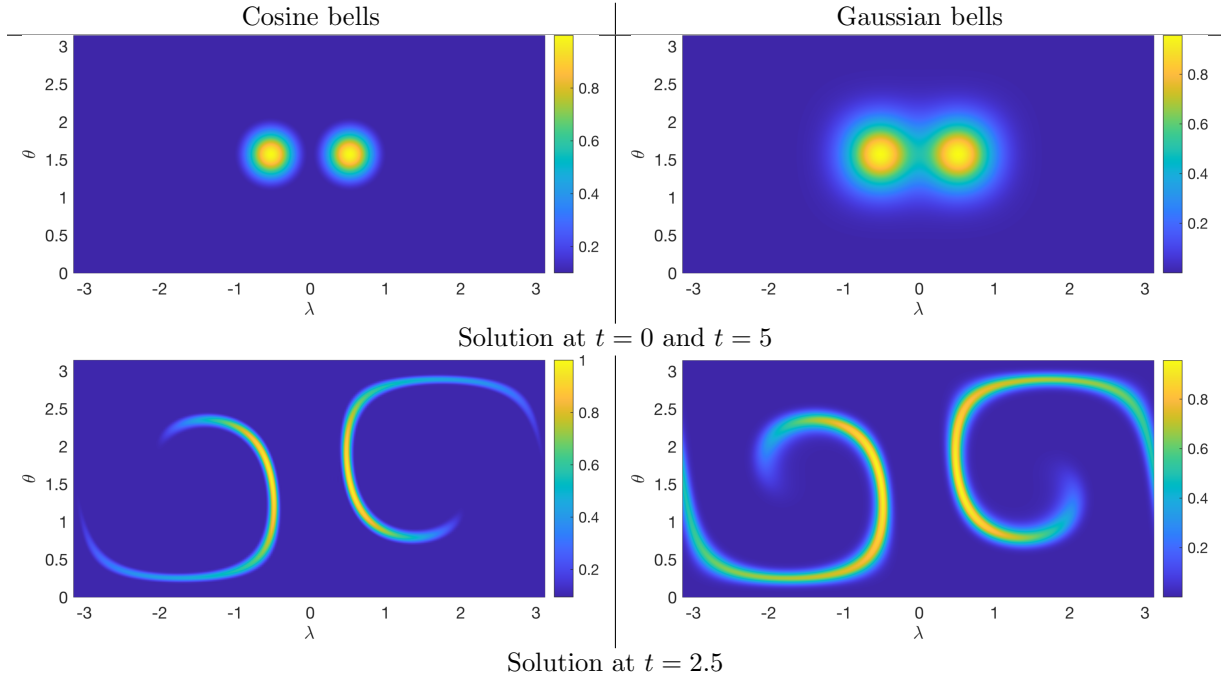


Figure 6: Illustrations of the solutions at $t = 0$, $t = 2.5$, and $t = 5$ (same as $t = 0$) for the deformational flow test case.

where u/v are components of the velocity field in longitude/latitude and $T = 5$. This velocity field translates and deforms the initial condition $q(\lambda, \theta, 0)$ up to time $t = 2.5$ and then reverses so that q is returned to its initial position and value at time $t = 5$, i.e., $q(\lambda, \theta, 0) = q(\lambda, \theta, 5)$. The initial condition then serves as the exact solution for comparing the numerical solutions at $t = 5$. We consider the following two initial conditions for the experiments:

- *Cosine bells:* $q(\lambda, \theta, 0) = 0.1 + 0.9(q_1(\lambda, \theta) + q_2(\lambda, \theta))$, where for $i = 1, 2$

$$q_i(\lambda, \theta) = \begin{cases} \frac{1}{2} (1 + \cos(2\pi \arccos(r_i(\lambda, \theta)))) & \arccos(r_i(\lambda, \theta)) < \frac{1}{2}, \\ 0 & \text{otherwise.} \end{cases}$$

- *Gaussian bells:* $q(\lambda, \theta, 0) = 0.95 (e^{-10(1-r_1(\lambda, \theta))} + e^{-10(1-r_2(\lambda, \theta))})$.

Here $r_i(\lambda, \theta) = \cos(\theta) \cos(\theta_i) + \cos(\lambda - \lambda_i) \sin(\theta) \sin(\theta_i)$, $i = 1, 2$, and the centers of the bells are given as $(\lambda_1, \theta_1) = (\pi/6, 0)$ and $(\lambda_2, \theta_2) = (-\pi/6, 0)$. The first initial condition is only $C^1(\mathbb{S}^2)$ and is meant to test the dispersive errors of a numerical solver, while the second is $C^\infty(\mathbb{S}^2)$ and is meant

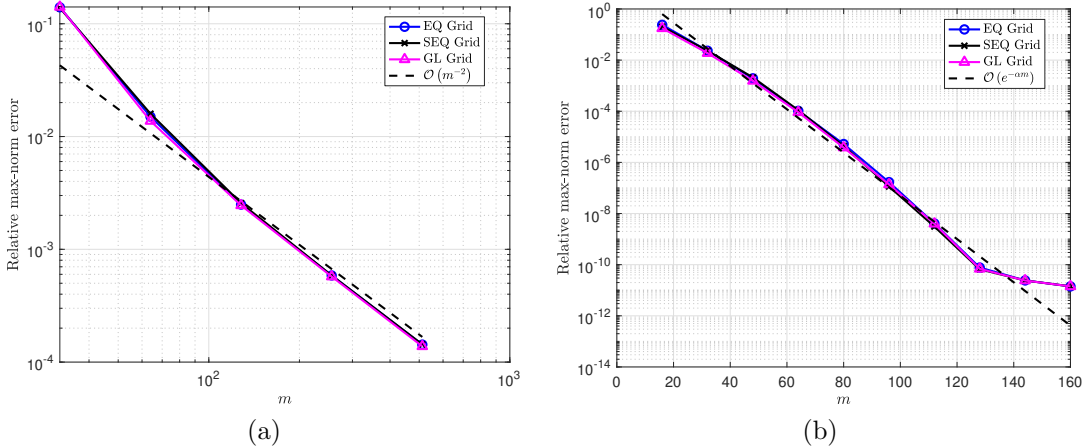


Figure 7: Spatial convergence results for (a) the cosine bells test case using a time-step equal to $10 \times \text{CFL}$ and (b) the Gaussian bells test case using a time-step equal to CFL . All the grid types use $2m$ points in longitude and $n = m + 1$ in latitude. Note (a) is plotted on a loglog scale while (b) is plotted on a semilogy scale and both plots display estimates of convergence rates as dashed lines.

to show the maximum convergence rate that is possible. Plots of the solutions of the deformational flow test case at $t = 0, 2.5,$ and 5 are displayed in Figure 6.

We use all three common tensor-product spherical grids discussed in Section 3.1 in the experiments, with $2m$ points in longitude and $n = m + 1$ points in latitude, which gives the grid spacing in longitude as $h = \pi/m$. We select the SLA time-step in the experiments according to a fixed multiple of the CFL number, which we set to $h/\|\mathbf{u}\|_\infty$, where $\|\mathbf{u}\|_\infty = 2.93$. For the cosine bells tests we use a time-step 10 times the CFL number, while for the Gaussian bells tests we just use the CFL number. These values were chosen so that spatial errors dominate the computed solutions for most of the resolutions.

The relative max-norm errors of the numerical solutions from the experiments are plotted in Figure 7 as a function of the grid resolution m . For the cosine bells problem (see part (a) of the figure), we see that the errors are similar for all three grids and decrease as $\mathcal{O}(m^{-2})$ (or $\mathcal{O}(h^2)$). This algebraic rate is expected since the initial condition is only $C^1(\mathbb{S}^2)$. In contrast, we see that the errors decrease exponentially fast with m for the $C^\infty(\mathbb{S}^2)$ Gaussian bells initial condition, until temporal errors begin to dominate the computed solutions after $m = 128$.

Finally, we compare the accuracy of the new barycentric SLA method to other methods from the literature for this same test problem in Table 3. We see for the cosine bells test case that the new method compares favorably to all the methods and gives a slightly smaller error than the RBF-PU based SLA method for the same resolution and time-step. For the Gaussian bells problem, the new method clearly provides the best accuracy for comparable resolutions and time-steps to the other methods. The next lowest error is produced by the Global RBF method, which is also spectrally accurate. By doubling the time-step for the same resolution, the new method shows a further decrease in the errors indicating that temporal errors may still be dominating. It should be noted, however, that the CSLAM, DG, and HOMME methods are all mass-conserving, whereas, the present SLA method is not.

6 Concluding remarks

We have introduced new bivariate barycentric formulas for the sphere and disk based on the DFS method. These formulas are efficient in the sense that do not require a transform to trigonometric or polynomial coefficients, but instead work directly with the data and a set of weights that only depend on the grid. For many commonly used grids in applications, these weights are known explicitly or can be computed in a stable and efficient manner. The formulas also deliver high-order accuracy for

Method	Resolution (in degrees)	Degrees of freedom	Number of time-steps	Relative ℓ_2 error
Cosine Bells				
CSLAM [35]	0.75°	86400	240	$\approx 6 \times 10^{-3}$
DG, $p = 3$ [44]	1.5°	38400	2400	1.39×10^{-2}
RBF-PU [52], $n = 84$	1.5°	23042	35	3.63×10^{-3}
Global RBF [52]	1.64°	15129	45	5.10×10^{-3}
Barycentric DFS	1.5°	29040	35	3.25×10^{-3}
Gaussian Bells				
CSLAM [35]	0.75°	86400	240	$\approx 5 \times 10^{-4}$
HOMME, $p = 6$ [36]	1.5°	29400	4800	$\approx 3 \times 10^{-3}$
RBF-PU [52], $n = 84$	1.5°	23042	80	1.35×10^{-5}
Global RBF [52]	1.64°	15129	200	7.68×10^{-8}
Barycentric DFS	1.5°	29040	200	1.17×10^{-8}
Barycentric DFS	1.5°	29040	400	7.99×10^{-10}

Table 3: Comparison of the barycentric DFS-based SLA scheme using the EQ grid with various methods from the literature for the two deformational flow test cases. CSLAM refers to the conservative semi-Lagrangian multi-tracer transport scheme used in [35], which uses a cubed-sphere grid. DG is the discontinuous Galerkin scheme from [44], an Eulerian scheme employing $p = 3$ degree polynomials (fourth-order accurate) on a cubed-sphere grid. HOMME (High-Order Methods Modeling Environment) is an Eulerian scheme from [36], also using a cubed-sphere grid, with results shown for a continuous Galerkin formulation using $p = 6$ degree polynomials (seventh-order accurate). RBF-PU (partition of unity) and global RBF refer to SLA advection schemes based on radial basis function interpolation from [52]. Values marked with \approx were estimated from plots of the relative ℓ_2 errors in the referenced papers, as exact values were not provided. The results given for the CSLAM, DG, and HOMME methods correspond to the non-filtered (or non shape-preserving) versions, which yielded the lowest errors for these test cases. Resolution (in degrees) indicates the approximate spacing of grid points (or nodes) around the equator.

smooth solutions. Moreover, the formulas are straightforward to implement, making them practical for a wide range of applications.

The question of stability is more subtle, particularly given the results on the stability of trigonometric barycentric formulas in [3]. However, as noted in that study, the trigonometric barycentric formula remains stable in most practical situations. Whether this holds for the even/odd/ π -periodic/ π -anti-periodic trigonometric formulas used here remains an open question and warrants further investigation. Nevertheless, our extensive numerical testing of the formulas, including their application to SLA, revealed no stability issues in practice.

The application of these new barycentric formulas to SLA for the tracer transport problem on the sphere shows promising results. This technique compares favorably in terms of accuracy to existing methods, suggesting that further explorations on more complex atmospheric flows are justified.

Lastly, while this study focused on trigonometric and polynomial approximations for the sphere and disk, the resulting barycentric formulas could naturally extend to more general rational approximations. For example, the even/odd polynomial formulas used for the disk could employ more general Floater-Hormann linear barycentric rational formulas [20], or even AAA type formulas [45]. This would only require a different technique for computing the weights. Linear barycentric rational formulas have been used successfully for the disk and more general star-like domains in [8]. Similarly, the trigonometric formulas derived here for the sphere and disk could be extended to rational trigonometric formulas using any of the approaches from [4, 7, 61]. In one dimension, rational barycentric formulas provide a richer approximation space, particularly for functions with singularities, and we expect that this benefit will also extend to the sphere and disk.

Acknowledgements

The authors thank Anthony Austin for discussions about the π -antiperiodic barycentric interpolation formula discussed in Section 2.1 and Alex Townsend and Daniel Fortunato for discussions about using DFS-based interpolation formulas within the SLA framework for solving PDEs on the sphere. The authors work was partially supported by US National Science Foundation grants 1952674 and 2309712.

Conflict of Interest

The authors declare no conflict of interest.

References

- [1] J. C. ADAMS AND P. N. SWARZTRAUBER, *SPHEREPACK 3.0: A model development facility*, Mon. Wea. Rev., 127 (1999), pp. 1872–1878.
- [2] P. ALFELD, M. NEAMTU, AND L. L. SCHUMAKER, *Fitting scattered data on sphere-like surfaces using spherical splines*, Journal of Computational and Applied Mathematics, 73 (1996), pp. 5–43.
- [3] A. P. AUSTIN AND K. XU, *On the numerical stability of the second barycentric formula for trigonometric interpolation in shifted equispaced points*, IMA J. Numer. Anal., 37 (2017), pp. 1355–1374.
- [4] C. BANDIZIOL AND S. DE MARCHI, *On the Lebesgue constant of the trigonometric Floater-Hormann rational interpolant at equally spaced nodes*, Dolomites Research Notes on Approximation, 12 (2019).
- [5] R. BARTNIK AND A. NORTON, *Numerical methods for the Einstein equations in null quasi-spherical coordinates*, SIAM J. Sci. Comp., 22 (2000), pp. 917–950.
- [6] J.-P. BERRUT, *Baryzentrische formeln zur trigonometrischen interpolation (i)*, Zeitschrift für angewandte Mathematik und Physik ZAMP, 35 (1984), pp. 91–105.
- [7] J.-P. BERRUT AND G. ELEFANTE, *Bounding the lebesgue constant for a barycentric rational trigonometric interpolant at periodic well-spaced nodes*, Journal of Computational and Applied Mathematics, (2021), p. 113664.
- [8] ———, *A linear barycentric rational interpolant on starlike domains*, arXiv preprint arXiv:2104.09246, (2021).
- [9] J.-P. BERRUT AND L. N. TREFETHEN, *Barycentric Lagrange interpolation*, SIAM Rev., 46 (2004), pp. 501–517.
- [10] I. BOGAERT, *Iteration-free computation of Gauss–Legendre quadrature nodes and weights*, SIAM J. Sci. Comp., 36 (2014), pp. A1008–A1026.
- [11] J. P. BOYD, *The choice of spectral functions on a sphere for boundary and eigenvalue problems: A comparison of Chebyshev, Fourier and associated Legendre expansions*, Mon. Wea. Rev., 106 (1978), pp. 1184–1191.
- [12] ———, *Chebyshev and Fourier Spectral Methods*, Courier Corporation, 2001.
- [13] J. P. BOYD AND F. YU, *Comparing seven spectral methods for interpolation and for solving the Poisson equation in a disk: Zernike polynomials, Logan–Shepp ridge polynomials, Chebyshev–Fourier series, cylindrical Robert functions, Bessel–Fourier expansions, square-to-disk conformal mapping and radial basis functions*, J. Comput. Phys., 230 (2011), pp. 1408–1438.

-
- [14] B. BRÜGMANN, *A pseudospectral matrix method for time-dependent tensor fields on a spherical shell*, J. Comput. Phys., 235 (2013), pp. 216–240.
- [15] H.-B. CHEONG, *Application of double Fourier series to the shallow-water equations on a sphere*, J. Comput. Phys., 165 (2000), pp. 261–287.
- [16] C.-J. DE LA VALLÉE POUSSIN, *Sur la convergence des formules d'interpolation entre ordonnées équidistantes*, Acad. Roy. Belg. Bull. Cl. Sci., 1908 (1908), pp. 319–410.
- [17] T. A. DRISCOLL, N. HALE, AND L. N. TREFETHEN, eds., *Chebfun Guide*, Pafnuty Publications, Oxford, 2014.
- [18] H. EISEN, W. HEINRICHS, AND K. WITSCH, *Spectral collocation methods and polar coordinate singularities*, J. Comput. Phys., 96 (1991), pp. 241–257.
- [19] M. FALCONE AND R. FERRETTI, *Semi-Lagrangian Approximation Schemes for Linear and Hamilton–Jacobi Equations*, SIAM, Philadelphia, PA, 2013.
- [20] M. S. FLOATER AND K. HORMANN, *Barycentric rational interpolation with no poles and high rates of approximation*, Numer. Math., 107 (2007), pp. 315–331.
- [21] B. FORNBERG, *A pseudospectral approach for polar and spherical geometries*, SIAM J. Sci. Comp., 16 (1995), pp. 1071–1081.
- [22] B. FORNBERG AND N. FLYER, *A Primer on Radial Basis Functions with Applications to the Geosciences*, Society for Industrial and Applied Mathematics, Philadelphia, 2015.
- [23] D. FORTUNATO, *A high-order fast direct solver for surface PDEs*, SIAM J. Sci. Comp., 46 (2024), pp. A2582–A2606.
- [24] T. GERYA, *Introduction to numerical geodynamic modelling*, Cambridge University Press, New York, 2019.
- [25] P. GODON, *Numerical modeling of tidal effects in polytropic accretion disks*, Astrophys. J., 480 (1997), p. 329.
- [26] T. HAIDEN, M. JANOUSEK, J. BIDLOT, L. FERRANTI, F. PRATES, F. VITART, P. BAUER, AND D. RICHARDSON, *Evaluation of ECMWF forecasts, including the 2016 resolution upgrade*, European Centre for Medium Range Weather Forecasts Reading, UK, 2016.
- [27] G. J. HALTINER AND R. T. WILLIAMS, *Numerical Prediction and Dynamic Meteorology*, John Wiley and Sons, New York, second ed., 1980.
- [28] Y. HAN, Y. HU, P. ZHANG, AND L. ZHANG, *Transition pathways between defect patterns in confined nematic liquid crystals*, J. Comput. Phys., 396 (2019), pp. 1–11.
- [29] W. HEINRICHS, *Spectral collocation schemes on the unit disc*, J. Comput. Phys., 199 (2004), pp. 66–86.
- [30] P. HENRICI, *Barycentric formulas for interpolating trigonometric polynomials and their conjugates*, Numer. Math., 33 (1979), pp. 225–234.
- [31] A. R. HERYUDONO AND T. A. DRISCOLL, *Radial basis function interpolation on irregular domain through conformal transplantation*, J. Sci. Comp., 44 (2010), pp. 286–300.
- [32] N. J. HIGHAM, *The numerical stability of barycentric Lagrange interpolation*, IMA J. Numer. Anal., 24 (2004), pp. 547–556.
- [33] W. HU AND S. DODELSON, *Cosmic microwave background anisotropies*, Annual Review of Astronomy and Astrophysics, 40 (2002), pp. 171–216.

-
- [34] A. J. JANSSEN AND P. DIRKSEN, *Computing Zernike polynomials of arbitrary degree using the discrete Fourier transform*, Journal of the European Optical Society-Rapid publications, 2 (2007).
- [35] P. H. LAURITZEN, W. C. SKAMAROCK, M. J. PRATHER, AND M. A. TAYLOR, *A standard test case suite for two-dimensional linear transport on the sphere*, Geosci. Model Dev., 5 (2012), pp. 887–901.
- [36] P. H. LAURITZEN, P. A. ULLRICH, C. JABLONOWSKI, P. A. BOSLER, D. CALHOUN, A. J. CONLEY, T. ENOMOTO, L. DONG, S. DUBEY, O. GUBA, A. B. HANSEN, E. KAAS, J. KENT, J.-F. LAMARQUE, M. J. PRATHER, D. REINERT, V. V. SHASHKIN, W. C. SKAMAROCK, B. SØRENSEN, M. A. TAYLOR, AND M. A. TOLSTYKH, *A standard test case suite for two-dimensional linear transport on the sphere: results from a collection of state-of-the-art schemes*, Geosci. Model Dev., 7 (2014), pp. 105–145.
- [37] A. T. LAYTON AND W. F. SPOTZ, *A semi-lagrangian double Fourier method for the shallow water equations on the sphere*, J. Comput. Phys., 189 (2003), pp. 180–196.
- [38] D. LEVIN, *The approximation power of moving least-squares*, Mathematics of computation, 67 (1998), pp. 1517–1531.
- [39] V. N. MAHAJAN AND G.-M. DAI, *Orthonormal polynomials in wavefront analysis: analytical solution*, JOSA A, 24 (2007), pp. 2994–3016.
- [40] G. MAI, Y. XUAN, W. ZUO, K. JANOWICZ, AND N. LAO, *Sphere2Vec: Multi-scale representation learning over a spherical surface for geospatial predictions*, 2022.
- [41] P. E. MERILEES, *The pseudospectral approximation applied to the shallow water equations on a sphere*, Atmosphere, 11 (1973), pp. 13–20.
- [42] S. MILDENBERGER AND M. QUELLMALZ, *Approximation properties of the double Fourier sphere method*, J. Fourier. Anal. Appl., 28 (2022), pp. 1–30.
- [43] ———, *A double Fourier sphere method for d-dimensional manifolds*, Sampl. Theory Signal Process. Data Anal., 21 (2023), p. 23.
- [44] R. D. NAIR AND P. H. LAURITZEN, *A class of deformational flow test cases for linear transport problems on the sphere*, J. Comput. Phys., 229 (2010), pp. 8868–8887.
- [45] Y. NAKATSUKASA, O. SÈTE, AND L. N. TREFETHEN, *The AAA algorithm for rational approximation*, SIAM J. Sci. Comp., 40 (2018), pp. A1494–A1522.
- [46] S. A. ORSZAG, *Fourier series on spheres*, Mon. Wea. Rev., 102 (1974), pp. 56–75.
- [47] H. RITCHIE, C. TEMPERTON, A. SIMMONS, M. HORTAL, T. DAVIES, D. DENT, AND M. HAMRUD, *Implementation of the semi-lagrangian method in a high-resolution version of the ecmwf forecast model*, Monthly Weather Review, 123 (1995), pp. 489–514.
- [48] D. RUIZ-ANTOLIN AND A. TOWNSEND, *A nonuniform fast Fourier transform based on low rank approximation*, SIAM J. Sci. Comp., 40 (2018), pp. A529–A547.
- [49] H. E. SALZER, *Coefficients for facilitating trigonometric interpolation*, J. Math. Phys., 27 (1948), pp. 274–278.
- [50] N. SCHAEFFER, *Efficient spherical harmonic transforms aimed at pseudospectral numerical simulations*, Geochemistry, Geophysics, Geosystems, 14 (2013), pp. 751–758.
- [51] L. L. SCHUMAKER, *Spline Functions*, SIAM, 2015.
- [52] V. SHANKAR AND G. B. WRIGHT, *Mesh-free semi-Lagrangian methods for transport on a sphere using radial basis functions*, J. Comput. Phys., 366 (2018), pp. 170–190.

-
- [53] J. SHEN, *A new fast Chebyshev–Fourier algorithm for Poisson-type equations in polar geometries*, Appl. Numer. Math., 33 (2000), pp. 183–190.
- [54] J. SŁOMKA, A. TOWNSEND, AND J. DUNKEL, *Stokes’ second problem and reduction of inertia in active fluids*, Physical Review Fluids, 3 (2018), p. 103304.
- [55] W. F. SPOTZ, M. A. TAYLOR, AND P. N. SWARZTRAUBER, *Fast shallow-water equation solvers in latitude-longitude coordinates*, J. Comput. Phys., 145 (1998), pp. 432–444.
- [56] A. STANFORTH AND J. CÔTÉ, *Semi-Lagrangian integration schemes for atmospheric models—a review*, Mon. Wea. Rev., 119 (1991), pp. 2206–2223.
- [57] W. TICHY, *Black hole evolution with the BSSN system by pseudospectral methods*, Phys. Rev. D, 74 (2006), pp. 1–10.
- [58] A. TOWNSEND, H. WILBER, AND G. B. WRIGHT, *Computing with functions in spherical and polar geometries I. the sphere*, SIAM J. Sci. Comp., 38 (2016), pp. C403–C425.
- [59] L. N. TREFETHEN, *Approximation Theory and Approximation Practice, Extended Edition*, SIAM, 2019.
- [60] H. WENDLAND, *Moving least squares approximation on the sphere*, Mathematical Methods for Curves and Surfaces, Vanderbilt Univ. Press, Nashville, TN, (2001), pp. 517–526.
- [61] H. WILBER, A. DAMLE, AND A. TOWNSEND, *Data-driven algorithms for signal processing with trigonometric rational functions*, SIAM J. Sci. Comp., 44 (2022), pp. C185–C209.
- [62] H. WILBER, A. TOWNSEND, AND G. B. WRIGHT, *Computing with functions in spherical and polar geometries II. the disk*, SIAM J. Sci. Comp., 39 (2017), pp. C238–C262.
- [63] G. B. WRIGHT, M. JAVED, H. MONTANELLI, AND L. N. TREFETHEN, *Extension of Chebfun to periodic functions*, SIAM J. Sci. Comp., 37 (2015), pp. C554–C573.
- [64] S. Y. YEE, *Studies on Fourier series on spheres*, Mon. Wea. Rev., 108 (1980), pp. 676–678.
- [65] H. YOSHIMURA, *Improved double Fourier series on a sphere and its application to a semi-implicit semi-Lagrangian shallow water model*, Geoscientific Model Development Discussions, 2021 (2021), pp. 1–53.
- [66] A. ZYGMUND, *Trigonometric series*, vol. 1, Cambridge University Press, 2002.